# Influence of Coastal Topography on Offshore Diurnal Rainfall Propagation Dynamics: A Linear Gravity Wave Model Approach

ZiJian Chen,[a] Yu Du,[a,b,c] Claire Vincent,[d,e] Ewan Short,[d,e] and Hongpei Yang[a]

[a] *School of Atmospheric Sciences, Sun Yat-sen University, and Southern Marine Science and Engineering Guangdong Laboratory (Zhuhai), Zhuhai, China*
[b] *Guangdong Province Key Laboratory for Climate Change and Natural Disaster Studies, Sun Yat-sen University, Zhuhai, China*
[c] *Key Laboratory of Tropical Atmosphere-Ocean System, Sun Yat-sen University, Ministry of Education, Zhuhai, China*
[d] *School of Geography, Earth and Atmospheric Sciences, The University of Melbourne, Melbourne, Victoria, Australia*
[e] *ARC Centre of Excellence for Climate Extremes, The University of Melbourne, Melbourne, Victoria, Australia*

(Manuscript received 30 September 2024, in final form 5 June 2025, accepted 23 June 2025)

ABSTRACT: The diurnal cycle is a fundamental driver of offshore rainfall propagation, with diurnal thermally forced gravity waves playing a primary role in triggering convection that propagates offshore. In this study, we conducted a series of idealized simulations using a simplified mesoscale model with varying terrain to investigate the influence of coastal topography on diurnally forced gravity waves. Our findings indicate that coastal topography increases the vertical length scale of diurnal heating near the coastline, resulting in gravity waves with a larger vertical wavelength scale and amplitude, and a faster phase speed, thereby altering the propagation speed of offshore rainfall. Based on this finding, we extended a two-dimensional linear land–sea-breeze analytical model by modifying the vertical heating forcing to account for the effect of coastal mountainous terrain. Our results demonstrate that higher coastal terrain significantly enhances the amplitude and horizontal and vertical wavelengths of inertia–gravity waves, successfully capturing the variations in phase speed associated with coastal topography.

SIGNIFICANCE STATEMENT: This study advances our understanding of the impact of coastal topography on inertia–gravity waves within a linear theoretical model framework. Through comparing idealized numerical simulations with varying coastal terrain heights to our newly developed linear theory, we provide deeper insights into the underlying dynamics. Our results suggest that coastal mountains amplify the horizontal and vertical wavelengths of gravity waves, increase wave amplitudes, and raise phase speeds. This novel linear theory is the first to incorporate the combined effect of mountain–plain thermal contrast and land–sea thermal contrast in coastal regions. It fills a gap in understanding the influence of coastal topography on the generation and characteristics of gravity waves. These modified wave properties directly affect the diurnal offshore propagation of rainfall, expanding our knowledge of coastal precipitation patterns. The results are significant as they reveal the sensitivity of coastal rainfall to the land–mountain–sea temperature gradient, a factor of relevance to tropical coastal communities in both current and future climates.

KEYWORDS: Inertia-gravity waves; Diurnal effects; Precipitation; Sea breezes; Valley/mountain flows

## 1. Introduction

Diurnal heating is a critical driver of land–sea circulation, profoundly influencing the balance and exchange of moisture and energy in coastal regions. This cyclic thermal forcing mechanism underpins a range of local- and regional-scale atmospheric and oceanic phenomena, including extreme coastal precipitation, wind-driven ocean currents, and land–sea breeze (Qian et al. 2009, 2012). Land breezes and sea breezes, one of the oldest phenomena studied in meteorology (Halley 1686; Rotunno 1983), have significant impacts on weather, climate, and wind energy potential (Jiang 2012a). They are closely related to density currents, coastal jets, coastal precipitation, and inertia–gravity waves, demonstrating the complexity and richness of the land–sea-breeze system and its interactions with local meteorology and topography.

In many tropical locations, squall lines are seen propagating away from the coast during the night and early morning, leading to a diurnal peak in precipitation in early morning over coastal water (Houze et al. 1981; Mori et al. 2004). This phenomenon of diurnal offshore propagation of rainfall has been observed along approximately 78% of the world's coastlines, particularly in low-latitude regions (equatorward of 30° latitude) where it is closely associated with density currents (or cold pools) and inertia–gravity waves driven by land–sea thermal contrast or land-based convection (Fang and Du 2022; Peatman et al. 2023). Numerous observational and numerical studies have highlighted the critical role of these waves in initiating offshore convection and precipitation propagation (e.g., Yang and Slingo 2001; Mapes et al. 2003a,b; Fang and Du 2022). Mapes et al. (2003b) suggested that offshore convection is likely associated with a diurnal gravity wave response to the oscillating heat source in the mixed layer, which is elevated into the stratified layers of the atmosphere by terrain. Offshore propagation of rainfall preferentially occurs near coastal mountain ranges, such as along the eastern coast

---

*Corresponding author*: Yu Du, duyu7@mail.sysu.edu.cn

DOI: 10.1175/JAS-D-24-0214.1

of India (Li and Carbone 2015; Peng and Chen 2023; Chen and Du 2024, hereafter CD24), the western coast of Mexico and Colombia (Li and Carbone 2015), the western coast of Sumatra (Ruppert et al. 2020; Peatman et al. 2023), the western coast of Puerto Rico (Sakaeda et al. 2024), and the northern coast of New Guinea (Vincent and Lane 2016).

In relation to the above findings, the following studies suggest that coastal topography plays a crucial role in triggering diurnal rainfall propagation and shaping its characteristics. Hassim et al. (2016) emphasized the importance of terrain and coastal effects, along with gravity waves, in contributing to the diurnal cycle over the Maritime Continent and suggested that elevated diabatic heating associated with convection over the land modifies the characteristics of the offshore propagation. A recent study by CD24 suggests that higher coastal mountains lead to increased propagation speed of rainfall due to a thicker heating depth near the coastline. The vertical scale of inertia–gravity waves forced by diurnal heating was found to be closely related to this heating depth. However, a clear and insightful understanding of the role of coastal mountains in affecting rainfall propagation is still lacking, especially from an analytical approach that allows for a deeper understanding of the underlying mathematical physics (Du et al. 2024).

Numerous studies have investigated these waves using linear theoretical models. Sun and Orlanski (1981) first discussed these waves in the context of a linear land–sea-breeze model. Rotunno (1983) emphasized that the atmospheric response takes the form of inertia–gravity waves at latitudes less than 30°, where the Coriolis parameter $f$ is smaller than the diurnal frequency $\omega$, using the linear land–sea-breeze theory. Subsequent research expanded on this linear theory in various aspects, including background wind, buoyancy frequency, and friction. Qian et al. (2009) and Du and Rotunno (2018) examined the effect of background wind, demonstrating Doppler shifting and associated wave dispersion. Du et al. (2019) investigated the impact of vertical wind shear on wave characteristics. Jiang (2012a,b) extended the linear theory to three dimensions, focusing on complex coastline shapes, stability, and boundary layer friction. Short et al. (2023) further developed the linear theory by incorporating linear changes in stability over a finite-depth "transition layer" between the boundary layer and troposphere. Peng and Chen (2024) extended the linear model numerically, driven by realistic meteorological fields, to reproduce offshore-propagating signals in the Bay of Bengal.

Previous studies have attempted to incorporate terrain effects into linear theory. Qian et al. (2012) examined both linear and nonlinear dynamics of sea breezes in the presence of an inland plateau, illustrating terrain effects on land (sea) breeze fronts and density currents. Li and Carbone (2015) used a linear model forced by surface heating and elevated heating to separately investigate the influence of land–sea breeze and mountain–plain cases on precipitation propagation, discussing the combined effect of these two dynamical mechanisms in coastal mountain situations. Hu et al. (2024) considered a hollow heating pattern to mimic the thermal forcing related to mountains, investigating rainfall propagation downstream of large inland terrain. While the aforementioned studies have investigated mountain effects, they still have some limitations. Many of these studies have oversimplified the heating distribution of mountains, either by focusing solely on elevated heating at mountain tops or by using idealized Gaussian-shaped distributions with hollow rectangles. Few have adequately considered the complex vertical heating distribution of mountains as observed in real-world situations.

Directly investigating the structure of inertia–gravity waves affected by coastal mountains in real-world scenarios is challenging. Basic atmospheric variables such as vertical motion or potential temperature, commonly employed in gravity wave studies, are often insufficient for this purpose. This insufficiency stems from the complexity arising from noise introduced by convection, vertical wind shear, and multiple phases of intraseasonal variability, making it difficult to isolate wave characteristics in real simulations. Therefore, this study aims to thoroughly investigate how coastal mountains affect the characteristics of inertia–gravity waves and rainfall propagation through both an idealized model and a linear analytical model. This approach facilitates a focused examination of these phenomena, enhancing our understanding of the underlying mechanisms. The novel linear theory developed in this study addresses a gap in understanding the impact of coastal topography on the generation of gravity waves due to diurnal thermal contrast.

While other factors such as density currents or cold pools also play important roles in influencing precipitation propagation, previous studies have shown that these mechanisms primarily affect relatively slower, nearshore propagation (e.g., Ruppert and Zhang 2019; Fang and Du 2022). In this study, we focus on inertia–gravity waves to examine the faster and longer-lasting propagation patterns observed farther offshore, with particular emphasis on how coastal topography impacts gravity waves in offshore propagation of precipitation.

The remainder of this paper is organized as follows. Section 2 describes the idealized model configuration and discusses the coastal terrain effect on gravity waves in idealized simulations. Section 3 establishes a linear theory including terrain consideration. Section 4 describes the characteristics of gravity waves associated with coastal topography derived from the linear analytical model. Finally, section 5 provides a summary and discussion of our findings.

## 2. Idealized simulations of gravity waves modulated by coastal topography

### a. Idealized mesoscale model configuration

CD24 suggested that higher coastal topography leads to faster propagation speed of rainfall as the vertical wavelength of gravity waves increases. However, this finding was drawn from semi-idealized, cloud-permitting numerical model experiments with realistic geography and correspondingly

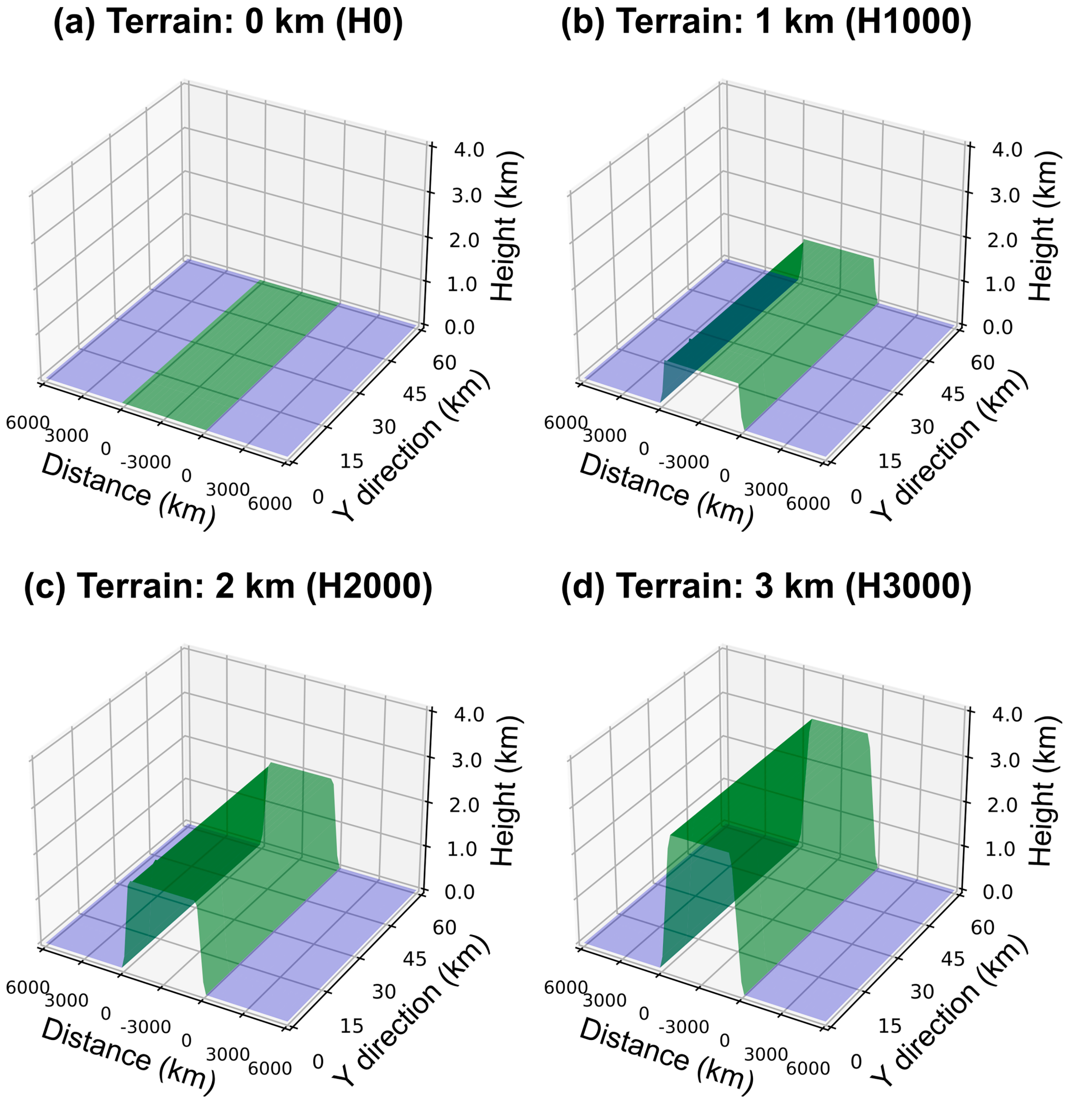

FIG. 1. Domain and terrain setting in WRF idealized experiments for (a) H0, (b) H1000, (c) H2000, and (d) H3000, with island (green shading) in the middle and the ocean (blue shading) elsewhere.

modified terrain, which may be influenced by unexpected factors such as complex small-scale topography. To further explore this conclusion, we perform idealized mesoscale model simulations with simplified terrain.

We use the Weather Research and Forecasting (WRF) Model, version 4.3.2 (Skamarock et al. 2008), to conduct a series of 3D idealized land–sea-breeze experiments with varying coastal topography. These experiments build on the work of Du and Rotunno (2015, hereafter DR15), who successfully modeled thermally driven diurnal winds and gravity waves in coastal areas. The aim is to study how coastal terrain influences the diurnal offshore propagation of gravity waves and associated rainfall. Although the model configuration closely follows that of DR15, it employs different grid resolutions and coastal mountain shapes as detailed below.

The model was configured with a 10-km horizontal grid spacing and 61 vertical levels[1] in a stretched grid configuration. The simulation domain measures 18 000 km in the *x* direction and 60 km in the *y* direction, featuring a 6000-km-wide island in the center and ocean on either side, as shown in Fig. 1. The

---

[1] $\eta$ levels: 1.000 000, 0.995 974, 0.990 156, 0.982 569, 0.973 242, 0.962 212, 0.949 522, 0.935 225, 0.919 382, 0.902 071, 0.883 377, 0.863 378, 0.842 161, 0.819 815, 0.796 436, 0.772 127, 0.746 990, 0.721 129, 0.694 651, 0.667 661, 0.640 266, 0.612 570, 0.584 674, 0.556 679, 0.528 682, 0.500 775, 0.473 046, 0.445 580, 0.418 457, 0.391 754, 0.365 542, 0.339 889, 0.314 859, 0.290 511, 0.266 905, 0.244 097, 0.222 144, 0.201 102, 0.181 030, 0.161 992, 0.144 080, 0.127 398, 0.112 046, 0.098 075, 0.085 462, 0.074 125, 0.063 965, 0.054 883, 0.046 785, 0.039 585, 0.033 202, 0.027 562, 0.022 594, 0.018 230, 0.014 411, 0.011 077, 0.008 177, 0.005 662, 0.003 487, 0.001 612, and 0.000 000.

top of the model domain is set at 50 hPa, with diffusion and implicit gravity wave damping layer (topmost 10 km) added to prevent reflections from the upper boundary. Following the configuration of EXP1 in DR15, no boundary layer, microphysics, radiation, and convective parameterization schemes are used in the simulations. Instead, the surface heat flux at the lower boundary is set as diurnal thermal forcing with an amplitude of 20 W $m^{-2}$, varied sinusoidally in time over land and fixed to zero over ocean. Vertical diffusion is set to 1 $m^2$ $s^{-1}$ for momentum and 6 $m^2$ $s^{-1}$ for heat, while horizontal diffusion of momentum and heat is set to zero. The model is initialized with constant static stability ($N = 0.00967$ $s^{-1}$) and no background wind. Each experiment runs for 20 days, with the first 10 days allocated for model spinup to achieve equilibrium, and the composite of the last 10 days used for the analysis. The Fourier transform magnitude spectrum from our simulations demonstrates that energy is predominantly concentrated in the 24-h mode (not shown), supporting our focus on investigating diurnal processes.

In our experiments, the island topography is modeled as an isosceles trapezoid, with a slope similar to that of the control (CTL) run in CD24. The influence of coastal mountains is examined for five different terrain top heights: 0, 500, 1000, 2000, and 3000 m, as illustrated in Fig. 1. Numerical simulations with different mountain heights are designated as H0, H500, H1000, H2000, and H3000, respectively. The result of H500 is shown only in Fig. 5 for comparison with the realistic model simulations from CD24. To reduce complexity, variations in mountain slope were not considered in this study.

### b. Model results

In this section, we examine how coastal mountains affect the propagation characteristics of gravity waves by comparing a series of sensitivity experiments involving varying terrain heights. The pattern of gravity waves is depicted in Hovmöller diagrams through hourly composites of vertical velocity anomalies $w'$, where $w' = w - \overline{w}$ and $\overline{w}$ is the time mean over the 10-day analysis period. And the vertical velocity anomalies $w'$ are averaged between 3 and 5 km above ground level (AGL; Fig. 2), as this is the layer where the main body of convection primarily occurs in CD24. The propagation of gravity waves exhibits an eastward phase speed of 9.8 m $s^{-1}$ based on $w'$ in the flat land experiment (H0; Fig. 2a).

The gravity waves in the other three experiments (H1000, H2000, and H3000; Figs. 2b–d) with coastal terrain propagate faster than those in H0, implying that the presence of topography enhances the phase speed of gravity waves. Consistent with the findings noted in CD24, the phase speed increases with the height of the coastal mountain. Specifically, the phase speed of 14.9 m $s^{-1}$ in H3000 is 1.6 m $s^{-1}$ faster than that in H2000 and 4.5 m $s^{-1}$ faster than that in H1000. These differences are attributed to the increase in vertical wavelength as gravity waves are generated by thicker heating depth from higher coastal mountains, as revealed in CD24.

It is also worth noting that the amplitudes of both the vertical velocity and temperature anomalies (not shown) strengthen with higher mountains. The maximum vertical velocity increases from around 0.02 m $s^{-1}$ in H0 to 0.18 m $s^{-1}$ in H3000. This result is not evident in the realistic model simulations of CD24. The exact cause of this amplitude increase will be discussed in the next part of the present study.

### c. Impact of coastal topography on inertia–gravity waves

To examine how the structure, phase speed, and amplitude of gravity waves are affected by coastal terrain, diurnal composite cross sections of vertical motion $w'$ are further provided (Fig. 3). Similar to the results shown in CD24 (their Fig. 7), $w'$ exhibits very prominent upward-tilted rays that appear to radiate offshore from the source at the coastline and along the mountain slope (Fig. 3). The ray paths extending shoreward and seaward in Fig. 3a are evidence of inertia–gravity waves generated by the diurnal land–sea thermal contrast, as mentioned in Rotunno (1983) and observed in several previous modeling studies (Birch et al. 2016; Hassim et al. 2016; Vincent and Lane 2016).

Comparisons between experiments with flat plain coast (Fig. 3a) and those featuring coastal mountains (Figs. 3b–d) suggest that the vertical scale of inertia–gravity waves triggered by the coastal area increases, and their amplitude intensifies, with increasing terrain height. These results imply that the higher elevation contributes to increasing the heating depth around coastal areas, leading to inertia–gravity waves with larger vertical wavelengths. This finding aligns with the results presented in CD24.

The ascending phase of gravity waves in all simulations appears at around time 19 from the coastline and then propagates seaward. These upward motions caused by gravity waves tend to drive nocturnal offshore-propagating precipitation over the ocean (Mapes et al. 2003b; Li and Carbone 2015; Peng and Chen 2023; CD24). The amplitude of inertia–gravity waves also increases with mountain height, which may be due to the larger heating area of the slope from the higher coastal mountain, containing more thermal energy to excite stronger gravity waves.

As coastal terrain increases, the structure of gravity waves shifts from thinner to thicker ray paths in response to changes in the heating source. Following Fig. 11 in CD24, we calculate the vertical wavelength in all experiments using vertical fluctuations in $w'$ to illustrate the relationship between coastal terrain height and the dominant vertical wavelength of the gravity wave spectrum. Specifically, we identify the distance between two consecutive zero points (where $w' = 0$) in the vertical profiles of $w'$ from each model column over the ocean from 150 to 900 km in Fig. 3. This range is chosen to focus on the influence of gravity waves while excluding the effects of density currents near the coast (0–150 km) (Hassim et al. 2016; Fang and Du 2022). This distance represents half of the vertical wavelength of the inertia–gravity waves. These waves are primarily excited by the thermal contrast at the coastline, while the coastal slope may influence wave characteristics. The analysis is conducted from the surface up to 10-km

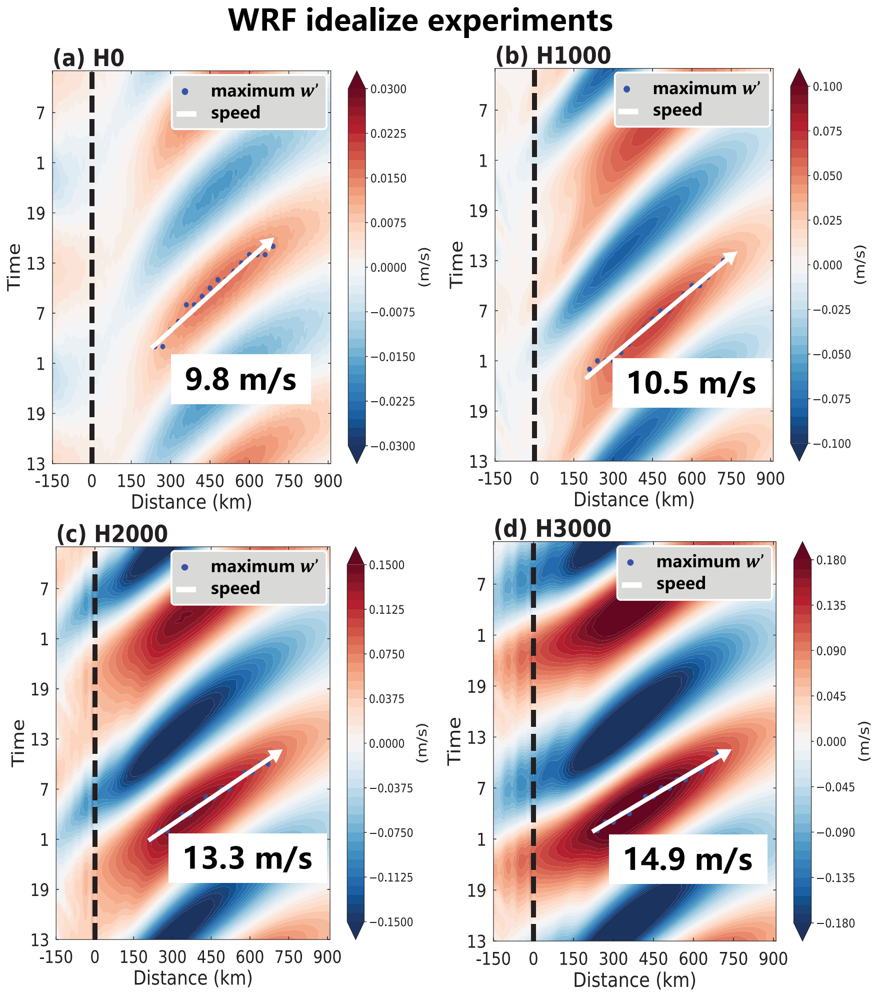

FIG. 2. Diurnal composite Hovmöller diagrams of the time-mean subtracted vertical velocity $w'$ (m $s^{-1}$; shaded) vertically averaged from 3 to 5 km AGL for days 10–20 from (a) H0, (b) H1000, (c) H2000, and (d) H3000. The white solid line indicates the propagation speed (m $s^{-1}$), the blue dots indicate the maximum $w'$, and the black dash line indicates the location of the coastline.

altitude. Comparing to Fourier decomposition, this method can accurately resolve vertical wavelengths in the limited vertical domain of our study.

Probability density functions (PDFs) of the vertical wavelength from idealized simulations are presented in Fig. 4, using the method described above. The distribution reflects the set of vertical wavelengths calculated at all locations from 150 to 900 km from the coast. A comparison of H0 with other experiments reveals that coastal mountains play an important role in enhancing the vertical wavelength of gravity waves excited by coastal diurnal forcing, thereby confirming that the higher elevation deepens the heating depth over the coastal mountain area.

The sensitivity experiments with varying mountain heights (H0, H1000, H2000, and H3000) quantitatively provide a robust relationship between vertical wavelength of gravity waves and coastal mountain height (Fig. 4). The dominant vertical wavelength is 5.3 km in H1000 with a 1-km height mountain, and it increases to 6.4 and 7.5 km with 2-km height and 3-km height mountains, respectively. Here, the dominant vertical wavelength is defined as the maxima of the wavelength PDF. As mountain height increases, the dominant vertical wavelength shows a nonlinear growth pattern. For lower mountain heights (below 1 km), the increase in vertical wavelength is relatively slow. However, as mountain height continues to rise, the rate of increase accelerates. Overall, for each 1-km increase in mountain height, the dominant vertical wavelength rises by 0.8–1.1 km, with larger increases occurring at greater mountain heights. This trend suggests a progressive amplification of the relationship between mountain height and vertical wavelength as the topography becomes more elevated. This intriguing relationship supports the hypothesis of CD24 that offshore propagation of rainfall is sensitive to coastal terrain.

Vertical profiles of the potential temperature anomaly in the idealized experiments are shown in Fig. 5a. These profiles

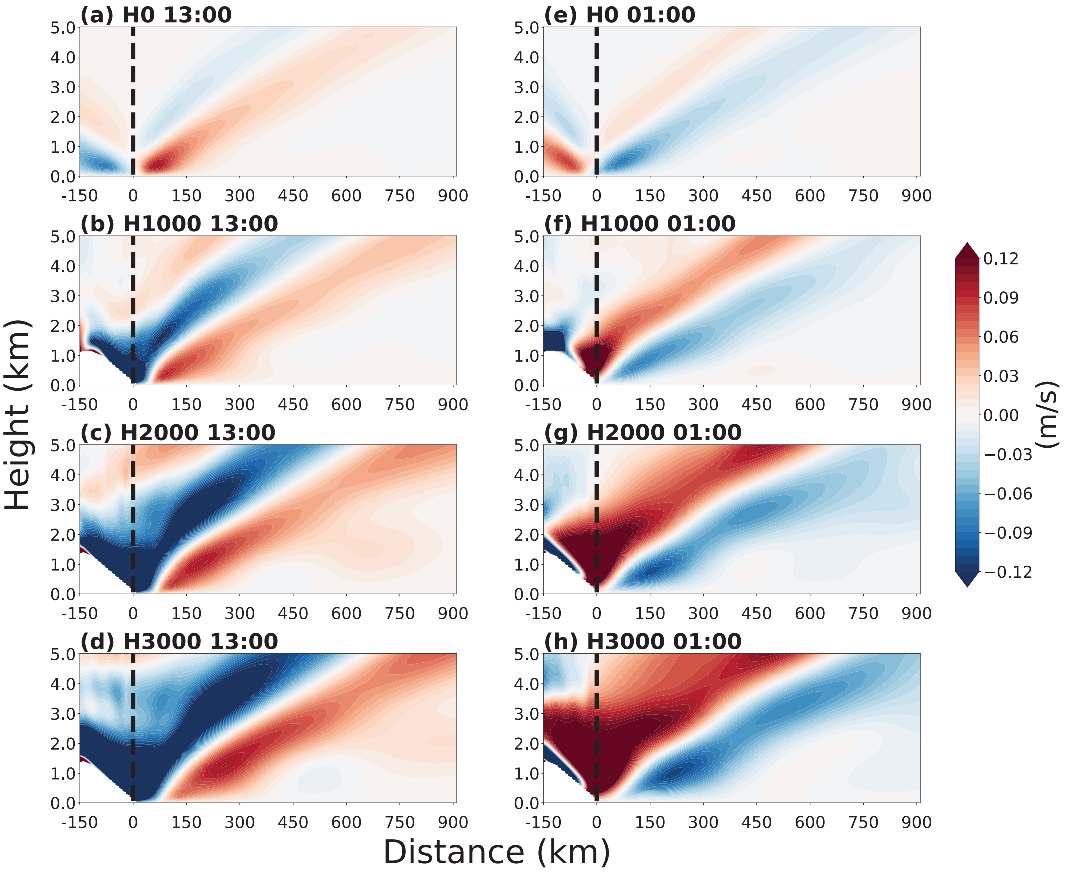

FIG. 3. Diurnal composite cross sections of the time-mean subtracted vertical velocity $w'$ (m s$^{-1}$; shaded) for days 10–20 from (a),(e) H0, (b),(f) H1000, (c),(g) H2000, and (d),(h) H3000 at times 0100 and 1300 local time (LT). The black dashed line indicates the location of the coastline.

are averaged over the coastal area, including the mountain slope, and display the difference between daytime (times 0600–1800 LT) and nighttime (times 1800–0600 LT). In H0, the potential temperature anomaly decreases from the surface and approaches 0 K at around 500 m (blue line in Fig. 5a). In H1000, the profile decreases slowly from the surface to around the mountain top (1 km) and then decreases rapidly to 0 K at around 1500 m (green line in Fig. 5a). The profiles for other mountain heights (H2000 and H3000) show similar characteristics (not shown), indicating that the near-surface heating depth over coastal areas become deeper due to the presence of coastal topography. As we will show in section 3, with a

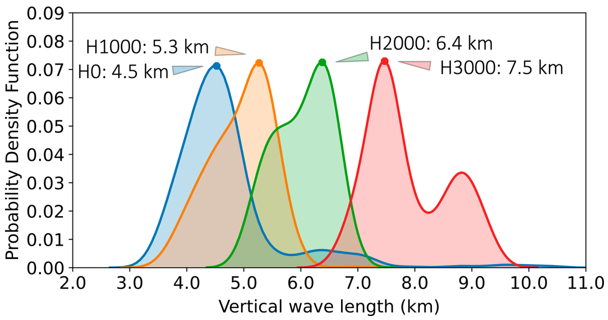

FIG. 4. PDFs of vertical wavelengths averaged over the ocean (0–900 km) from H0 (blue line), H1000 (orange line), H2000 (green line), and H3000 (red line), with dominant vertical wavelengths of 4.5, 5.3, 6.4, and 7.5 km, respectively.

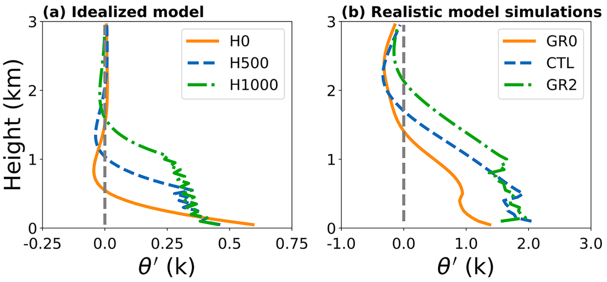

FIG. 5. Vertical profiles of the difference in diurnal composites of potential temperature anomalies near the coastline between daytime (times 0600–1800 LT) and nighttime (times 1800–0600 LT), horizontally averaged from −150 to 0 km relative to the coast. Results are shown for (a) idealized experiments in this study and (b) realistic model simulations in CD24, with average coastal mountain height of around 0 (GR0), 500 (CTL), and 1000 m (GR2).

thicker heating depth, the vertical scale of inertia–gravity waves becomes larger, resulting in faster phase speeds which govern the offshore propagation pattern of rainfall.

Figure 5b presents vertical profiles of potential temperature anomalies from the more realistic simulation experiments of CD24, complementing the idealized cases shown in Fig. 5a. In CD24, the average coastal mountain height is approximately 500 m in CTL, 1000 m in GR2, and 0 m in GR0. The profiles in the realistic model simulations (Fig. 5b) and the idealized cases (Fig. 5a) exhibit comparable similarities in vertical variations: a gradual decrease from the surface, followed by a rapid decline from the mountain top to the midtroposphere. It is noted that there is a more gradual decrease above the mountain top in realistic model simulations compared to that in idealized cases (Fig. 5a). This difference may be attributed to variations in the vertical diffusion coefficient within the boundary layer, as the idealized simulations lack a planetary boundary layer parameterization scheme. Alternatively, it could result from latent heat release in convective systems over land in the real-case experiments.

These findings support the hypothesis that coastal terrain significantly influences the phase speed of inertia–gravity waves, thereby affecting the propagation speed of rainfall. To provide deeper insights into the influence of coastal topography on the gravity waves, we extend the linear theory of the land–sea breeze to incorporate a heating profile similar to that depicted in Fig. 5. The previous study by Li and Carbone (2015) investigated the effect of coastal mountains using a linear theory with elevated heating, which did not adequately account for the heating induced by slope and land–sea thermal differences. Our newly developed linear theory aims to address these shortcomings and offer a more comprehensive understanding of how coastal topographic features impact gravity waves.

## 3. Linear analytical model with the impact of coastal topography

### a. Governing equations

The approximately two-dimensional equations of motion, derived using the Boussinesq approximation and incorporating friction and background winds, with an invariant $v^*$ wind component in the $y$ direction, can be written as follows (Ogura and Phillips 1962; Rotunno 1983; Qian et al. 2009; DR15; Du and Rotunno 2018; Du 2023; Short et al. 2023; Du et al. 2024):

$$\left(\frac{\partial}{\partial t^*} + U^*\frac{\partial}{\partial x^*}\right)u^* - f^*v^* = -\frac{\partial P^*}{\partial x^*} - \alpha^*u^*, \tag{1}$$

$$\left(\frac{\partial}{\partial t^*} + U^*\frac{\partial}{\partial x^*}\right)v^* + f^*u^* = -\alpha^*v^*, \tag{2}$$

$$\left(\frac{\partial}{\partial t^*} + U^*\frac{\partial}{\partial x^*}\right)w^* - b^* = -\frac{\partial P^*}{\partial z^*} - \alpha^*w^*, \tag{3}$$

$$\left(\frac{\partial}{\partial t^*} + U^*\frac{\partial}{\partial x^*}\right)b^* + N^{*2}w^* = Q^* - \alpha^*b^*, \tag{4}$$

$$\frac{\partial u^*}{\partial x^*} + \frac{\partial w^*}{\partial z^*} = 0, \tag{5}$$

where $u^*$, $v^*$, and $w^*$ represent the velocity perturbations in the $x^*$, $y^*$, and $z^*$ directions and $U^*$ is the uniform background wind in the $x^*$ direction. The $f^*$ represents the Coriolis parameter, $P^*$ is the Boussinesq disturbance pressure variable, $\alpha^*$ represents the friction coefficient ($10^{-11}$ s$^{-1}$), $b^*$ is the buoyancy, and $N^*$ represents the buoyancy frequency. Variables denoted with an asterisk ($^*$) represent dimensional quantities, while those without an asterisk represent their corresponding nondimensional counterparts.

Different from previous studies, the coastal topography heating function $Q^*$ (Fig. 6) is specified as

$$Q^* = \begin{cases} \dfrac{Q_0}{\pi}\left(\dfrac{\pi}{2} - \arctan\dfrac{x^*}{x_0^*}\right)e^{-[(z^*-H_m^*)/z_0^*]}\left(1 - \dfrac{H_m^*a}{z_0^*}\right)e^{-i\omega t^*} & \text{when } z^* \geq H_m^*, \\ \dfrac{Q_0}{\pi}\left(\dfrac{\pi}{2} - \arctan\dfrac{x^*}{x_0^*}\right)\left(1 - \dfrac{z^*a}{z_0^*}\right)e^{-i\omega t^*} & \text{when } z^* < H_m^*, \end{cases} \tag{6}$$

where $Q_0$ is the heating amplitude ($1.2 \times 10^{-5}$ m s$^{-3}$), $H_m$ is the height of coastal mountain, $z_0^* = 0.5$ km is the height scale, $x_0^*$ is the horizontal scale of land–sea contrast in heating, and $a$ represents the linear vertical decay rate of the heating function which describes the heating profile below the mountain height. The diurnal frequency $\omega = 2\pi/T$, where $T = 24$ h is the period of diurnal heating. In this study, $x^* = 0$ represents the coastline, with land and mountain to the left ($x^* < 0$) and sea to the right ($x^* > 0$). The buoyancy frequency ($N^* = 0.009\,67$ s$^{-1}$) is assumed to be constant here, which is calculated from that of the idealized simulation H0, as the average $N^*$ is similar across all idealized simulations.

Figure 6 presents examples of the heating function given by (6), with $x_0^* = 50$ km and $a = 0.125$. The heating function in Fig. 6a represents a land–sea thermal contrast over a flat coastal region, similar to the function used in Rotunno (1983), DR15, and Du and Rotunno (2018). In Figs. 6b–d, the effect of mountain slope on heating is included in the lower levels below $H_m^*$ (1 km in Fig. 6b, 2 km in Fig. 6c, and 3 km in Fig. 6d), exhibiting deeper heating layers near the surface.

The vertical profiles of the heating function, as given by (6) and averaged over the coastal area (from −150 to 0 km in Fig. 6), are shown in Fig. 7a. For the heating function in our

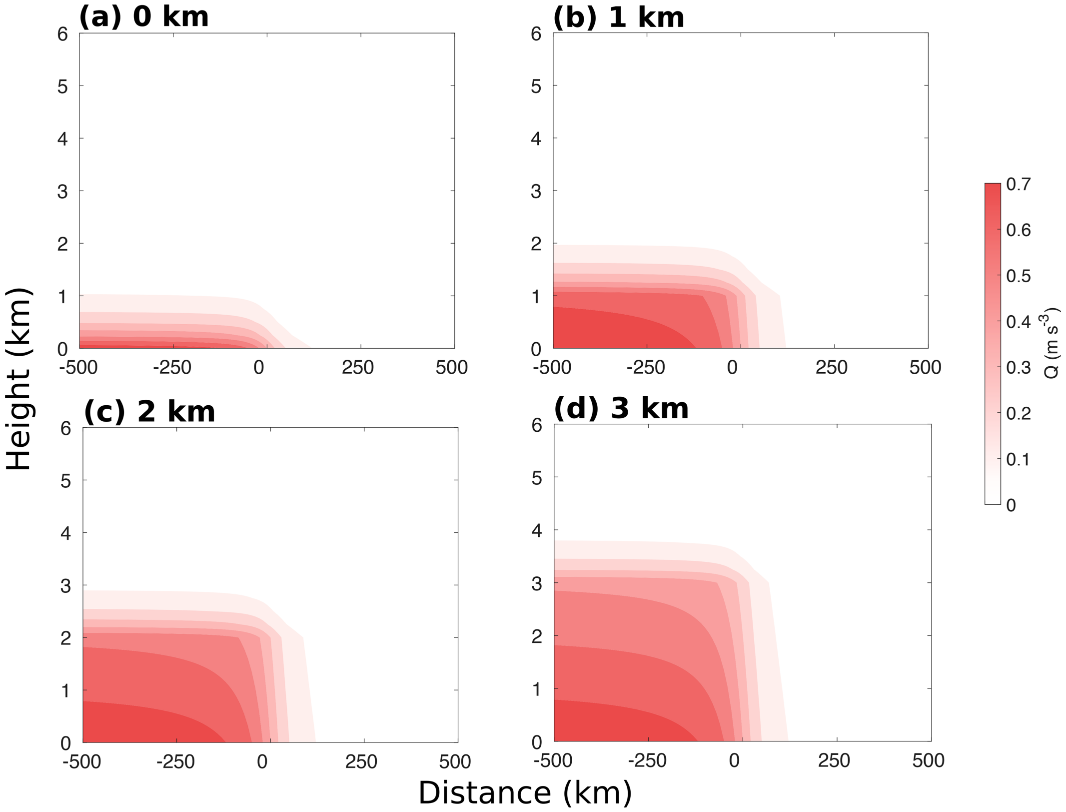

FIG. 6. The heating function $Q^* \times 10^5 (\mathrm{m\,s^{-3}})$ given by (6) for (a) $H_m^* = 0\,\mathrm{km}$, (b) $H_m^* = 1\,\mathrm{km}$, (c) $H_m^* = 2\,\mathrm{km}$, and (d) $H_m^* = 3\,\mathrm{km}$.

linear theoretical model, we make a simplified approximation based on the results of idealized simulations. The coastal land area, with its topography, is treated as a single unit (specifically, the region from −150 to 0 km in the idealized simulations). A representative vertical profile is derived by horizontally averaging the temperature distribution within this region. This averaged vertical profile is then incorporated into the heating function of the linear theoretical model to represent its vertical variation. This heating function consists of two components. Above the mountain top, we adopt an exponential decay heating function with height, following Rotunno 1983, using a boundary layer depth scale ($z_0^*$) of 0.5 to match the results from our idealized model. Below the mountain top, the heat decays linearly (Fig. 7a), which represents a weaker decay than the exponential function due to elevated heating effect of the terrain slope. The linear decay is consistent with the heating profiles observed in the idealized model (Fig. 7b).

It is important to note that the "blocking" effect of the mountain itself is ignored, and we use the boundary condition $w^*(z^* = 0) = 0$ in our linear model, as used in DR15. Figure 7a depicts various profiles: The orange line represents a flat coast area (0 km) with land–sea thermal contrast, similar to the scenario considered by Rotunno (1983), DR15, and Du and Rotunno (2018). The other profiles (blue, green, and red lines) include the heating effect of mountain slopes, extending to terrain height of 1, 2, and 3 km, respectively, illustrating progressively deeper heating layers near the surface.

Compared to the profiles in the idealized experiments (Fig. 7b), there are qualitative similarities and also notable differences. The profiles in the linear model are smoother, and the values are always positive. The nonsmooth profile below mountain height in the idealized simulations (Fig. 7b) possibly results from the coarse resolution of the model grid.

Next, the nondimensional dependent variables are defined as follows:

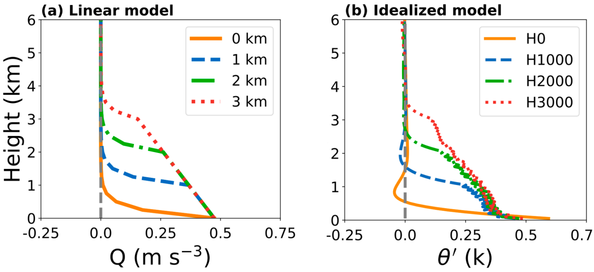

FIG. 7. As in Fig. 5, but for (a) the linear model with $H_m^* = 0$, 1, 2 and 3 km and (b) idealized experiments of H0, H1000, H2000, and H3000.

$$
\begin{aligned}
&x^* = Hx, && z^* = Hz, && t^* = \frac{t}{\omega}, && (u^*, v^*, w^*) = H\omega(u, v, w),\\
&b^* = H\omega^2 b, && P^* = H^2\omega^2 P, && f^* = \omega f, && \alpha^* = \omega\alpha,\ H_m^* = HH_m,\\
&Q^* = H\omega^3 Q, && U^* = H\omega U, && N^* = \omega N, && x_0^* = Hx_0,\ z_0^* = Hz_0,
\end{aligned}
\tag{7}
$$

where $H = 10$ km is the tropopause height (as in Du et al. 2024).

Rewriting (1)–(5) based on the above nondimensional variables, we obtain

$$\left(\frac{\partial}{\partial t} + U\frac{\partial}{\partial x} + \alpha\right)u - fv = -\frac{\partial P}{\partial x}, \tag{8}$$

$$\left(\frac{\partial}{\partial t} + U\frac{\partial}{\partial x} + \alpha\right)v + fu = 0, \tag{9}$$

$$\left(\frac{\partial}{\partial t} + U\frac{\partial}{\partial x} + \alpha\right)w - b = -\frac{\partial P}{\partial z}, \tag{10}$$

$$\left(\frac{\partial}{\partial t} + U\frac{\partial}{\partial x} + \alpha\right)b + N^2 w = Q, \tag{11}$$

$$\frac{\partial u}{\partial x} + \frac{\partial w}{\partial z} = 0. \tag{12}$$

### b. The analytical solution for gravity waves

Equations (8)–(12) can be combined into a single equation for the streamfunction $\psi$ ($u = \partial\psi/\partial z,\ w = -\partial\psi/\partial x$):

$$\left[\left(\frac{\partial}{\partial t} + U\frac{\partial}{\partial x} + \alpha\right)^2 + f^2\right]\frac{\partial^2\psi}{\partial z^2} + \left[N^2 + \left(\frac{\partial}{\partial t} + U\frac{\partial}{\partial x} + \alpha\right)^2\right]\frac{\partial^2\psi}{\partial x^2} = -\frac{\partial Q}{\partial x}. \tag{13}$$

Rewrite (6) as follows:

$$
Q = \begin{cases}
\dfrac{Q_0}{\pi H\omega^3}\left(\dfrac{\pi}{2} - \arctan\dfrac{x}{x_0}\right)\left(1 - \dfrac{za}{z_0}\right)e^{-it} & \text{when } z < H_m,\\[2ex]
\dfrac{Q_0}{\pi H\omega^3}\left(\dfrac{\pi}{2} - \arctan\dfrac{x}{x_0}\right)e^{-[(z-H_m)/z_0]}\left(1 - \dfrac{H_m a}{z_0}\right)e^{-it} & \text{when } z \geq H_m.
\end{cases}
\tag{14}
$$

Assume $\psi \propto \tilde{\psi}e^{-it}$, (13) and (14) can be combined into

$$
\begin{aligned}
&(A^2 + f^2)\frac{\partial^2\tilde{\psi}}{\partial z^2} + (A^2 + N^2)\frac{\partial^2\tilde{\psi}}{\partial x^2} = \frac{Q_0}{\pi H\omega^3}\,\frac{x_0}{x_0^2 + x^2}\left(1 - \frac{za}{z_0}\right) && \text{for } z < H_m,\\
&(A^2 + f^2)\frac{\partial^2\tilde{\psi}}{\partial z^2} + (A^2 + N^2)\frac{\partial^2\tilde{\psi}}{\partial x^2} = \frac{Q_0}{\pi H\omega^3}\,\frac{x_0}{x_0^2 + x^2}e^{-[(z-H_m)/z_0]}\left(1 - \frac{H_m a}{z_0}\right) && \text{for } z \geq H_m,
\end{aligned}
\tag{15}
$$

where $A = -i + U(\partial/\partial x) + \alpha$. Taking the Fourier transform of (15) in the $x$ direction with $\hat{\psi} = \int_{-\infty}^{\infty}\tilde{\psi}e^{-iKx}\,dx$, and letting $\sigma = 1 - KU + i\alpha$, (15) becomes

$$
\begin{aligned}
&(f^2 - \sigma^2)\frac{\partial^2\hat{\psi}}{\partial z^2} - (N^2 - \sigma^2)K^2\hat{\psi} = \frac{Q_0}{H\omega^3}e^{-x_0|K|}\left(1 - \frac{za}{z_0}\right) && \text{for } z < H_m,\\
&(f^2 - \sigma^2)\frac{\partial^2\hat{\psi}}{\partial z^2} - (N^2 - \sigma^2)K^2\hat{\psi} = \frac{Q_0}{H\omega^3}e^{-x_0|K|}\,e^{-[(z-H_m)/z_0]}\left(1 - \frac{H_m a}{z_0}\right) && \text{for } z \geq H_m.
\end{aligned}
\tag{16}
$$

Therefore, (16) can be written as

$$\frac{\partial^2\hat{\psi}}{\partial z^2} - \gamma^2\hat{\psi} = \hat{F}, \tag{17}$$

where

$$\gamma = \sqrt{\frac{(N^2 - \sigma^2)K^2}{f^2 - \sigma^2}}, \tag{18}$$

$$\hat{F} = \begin{cases}\hat{F}_1, & \text{for } z < H,\\ \hat{F}_2, & \text{for } z \geq H_m,\end{cases} \tag{19}$$

$$\hat{F}_1 = \frac{Q_0}{H\omega^3(f^2 - \sigma^2)}e^{-x_0|K|}\left(1 - \frac{za}{z_0}\right), \tag{20}$$

and

$$\hat{F}_2 = \frac{Q_0}{H\omega^3(f^2 - \sigma^2)} e^{-x_0|K|} e^{-[(z-H_m)/z_0]}\left(1 - \frac{H_m a}{z_0}\right). \qquad (21)$$

Note that when $f^2 < 1$, $U = 0$, and $\alpha = 0$, $\gamma$ is imaginary, and hence, $-\gamma^2$ is positive. Equation (17) then resembles the equation considered by Rotunno (1983) and Qian et al. (2009).

Following Rotunno (1983), Short et al. (2023), and Du et al. (2024), (17) may be solved using Green's method. First, define a Green function $G(k, z)$ satisfying

$$\frac{\partial^2 G}{\partial z^2} - \gamma^2 G = \delta(z - z'), \qquad (22)$$

representing the response to a point source at $z'$, where $\delta$ is the Dirac delta function. Considering the radiative upper-boundary condition (remains finite when $z \to \infty$) and that waves forced below $z'$ perfectly reflect off the lower-boundary condition, we obtain the solution for (22):

$$G(z, z') = \begin{cases} A\sinh\gamma z, & \text{for } z < z', \\ Be^{-\gamma z}, & \text{for } z > z'. \end{cases} \qquad (23)$$

Taking the boundary conditions that $G(z, z')$ is continuous at $z = z'$ and $\partial_z G(z'^{+}) - \partial_z G(z'^{-}) = 1$, we obtain

$$A\sinh\gamma z' = Be^{-\gamma z'} \qquad (24)$$

and

$$-\gamma Be^{-\gamma z'} - A\gamma\cosh\gamma z' = 1. \qquad (25)$$

Therefore, we have

$$A = -\frac{e^{-\gamma z'}}{\gamma} \qquad (26)$$

and

$$B = -\frac{\sinh\gamma z'}{\gamma}. \qquad (27)$$

Using Green's function, the solution for $\hat{\psi}$ can thus be summarized as

$$\hat{\psi} = e^{-\gamma z}\int_0^z -\frac{\sinh\gamma z'}{\gamma}\hat{F}_1\,dz' + \sinh\gamma z\int_z^{H_m} -\frac{e^{-\gamma z'}}{\gamma}\hat{F}_1\,dz' + \sinh\gamma z\int_{H_m}^{\infty} -\frac{e^{-\gamma z'}}{\gamma}\hat{F}_2\,dz' \qquad \text{for } z < H_m, \qquad (28)$$

$$\hat{\psi} = e^{-\gamma z}\int_0^{H_m} -\frac{\sinh\gamma z'}{\gamma}\hat{F}_1\,dz' + e^{-\gamma z}\int_{H_m}^{z} -\frac{\sinh\gamma z'}{\gamma}\hat{F}_2\,dz' + \sinh\gamma z\int_z^{\infty} -\frac{e^{-\gamma z'}}{\gamma}\hat{F}_2\,dz' \qquad \text{for } z \ge H_m. \qquad (29)$$

By integrating (28) and (29), we have

$$\hat{\psi} = \begin{cases} \dfrac{Q_0 e^{-x_0|K|}}{H\omega^3\gamma(\sigma^2 - f^2)}(I_1 + I_2 + I_3), & \text{for } z < H_m, \\ \dfrac{Q_0 e^{-x_0|K|}}{H\omega^3\gamma(\sigma^2 - f^2)}(I_4 + I_5 + I_6), & \text{for } z \ge H_m, \end{cases} \qquad (30)$$

where

$$I_1 = e^{-\gamma z}\frac{a\sinh\gamma z + \gamma(z_0 - az)\cosh\gamma z - \gamma z_0}{\gamma^2 z_0},$$

$$I_2 = \sinh\gamma z\frac{e^{-\gamma H_m}(aH_m\gamma + a - z_0\gamma) - e^{-\gamma z}(az\gamma + a - z_0\gamma)}{\gamma^2 z_0},$$

$$I_3 = \sinh\gamma z\frac{e^{-\gamma H_m}(z_0 - aH_m)}{z_0\gamma + 1},$$

$$I_4 = e^{-\gamma z}\frac{a\sinh\gamma H_m + \gamma(z_0 - aH_m)\cosh\gamma H_m - \gamma z_0}{\gamma^2 z_0},$$

$$I_5 = e^{-\gamma z}\frac{[e^{-(z-H_m/z_0)}(\gamma z_0\cosh\gamma z + \sinh\gamma z) - (\gamma z_0\cosh\gamma H_m + \sinh\gamma H_m)](z_0 - aH_m)}{\gamma^2 {z_0}^2 - 1}, \quad \text{and}$$

$$I_6 = \sinh\gamma z\frac{e^{[(H_m-z)/z_0]-\gamma z}(z_0 - aH_m)}{z_0\gamma + 1}.$$

Note that when $H_m = 0$, (30) can be summarized as

$$\hat{\psi} = \frac{Q_0 e^{-x_0|K|}{z_0}^2[e^{-(z/z_0)} - e^{-\gamma z}]}{H\omega^3(\sigma^2 - f^2)(\gamma^2 {z_0}^2 - 1)}, \qquad (31)$$

which represents the land–sea-breeze linear theory without terrain (Rotunno 1983; Qian et al. 2009; DR15; Du and Rotunno 2018).

Consequently, $\psi$ is then recovered from (30) using the inverse Fourier transform. We thus have

$$\psi = \mathrm{Re}\left\{\frac{1}{2\pi}\int_{-\infty}^{\infty}\hat{\psi}e^{i(Kx-t)}dK\right\}. \qquad (32)$$

According to the streamfunction, we obtain

$$u = \frac{\partial\psi}{\partial z} = \mathrm{Re}\left\{\frac{1}{2\pi}\int_{-\infty}^{\infty}\frac{\partial\hat{\psi}}{\partial z}e^{i(Kx-t)}dK\right\}, \qquad (33)$$

$$w = -\frac{\partial\psi}{\partial x} = \mathrm{Re}\left\{\frac{-i}{2\pi}\int_{-\infty}^{\infty}\hat{\psi}Ke^{i(Kx-t)}dK\right\}. \qquad (34)$$

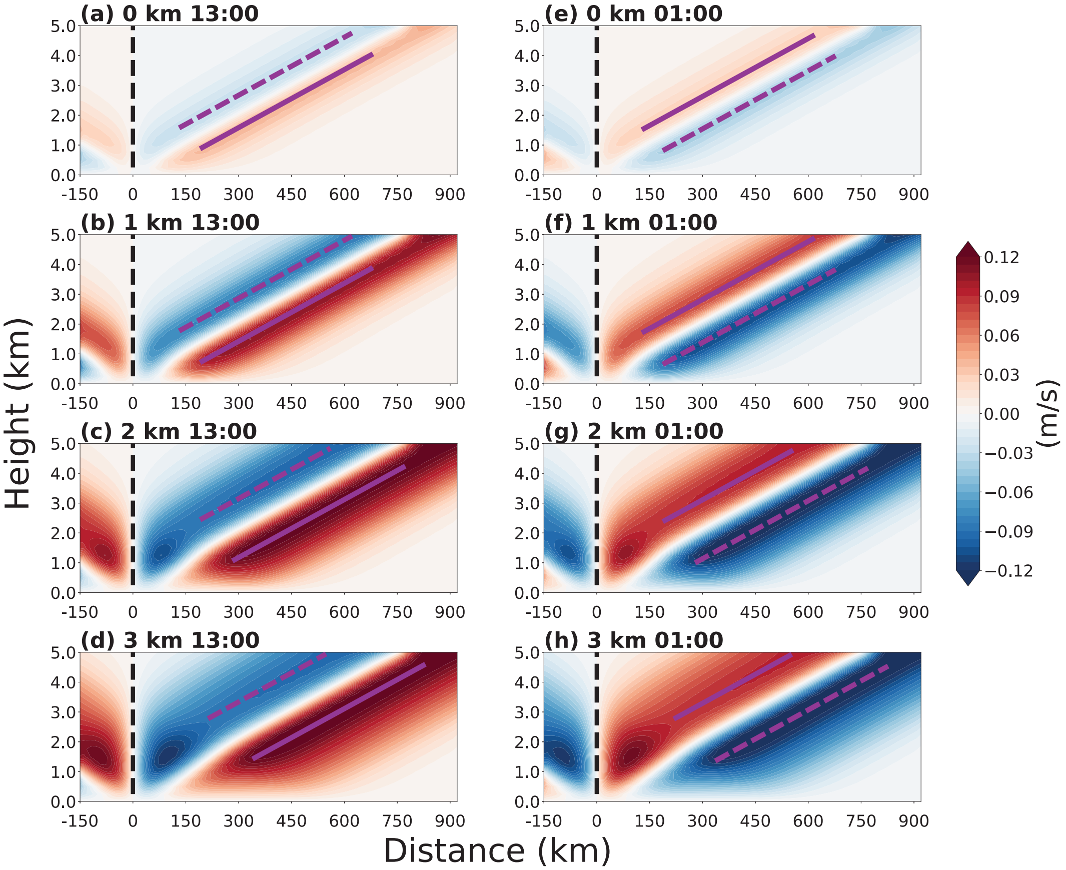

FIG. 8. As in Fig. 3, but for the linear model with (a),(e) $H_m^* = 0$ km, (b),(f) $H_m^* = 1$ km, (c),(g) $H_m^* = 2$ km, and (d),(h) $H_m^* = 3$ km. The solid (dashed) purple lines indicate the positive (negative) peak phase of gravity wave vertical motion.

The integrals in (33) and (34) are numerically evaluated using MATLAB in this study.

## 4. Gravity waves from the linear analytical model modulated by coastal topography

### *a. Gravity wave generation in flat coastal plains and varied coastal topography*

The structure of inertia–gravity waves generated from a flat coastal plain in the linear model is depicted in Figs. 8a and 8e through cross sections of vertical velocity, with $N^* = 0.009\,67\ \mathrm{s}^{-1}$ (averaged from H0 test), $z_0^* = 0.5$ km, $x_0^* = 50$ km, $a = 0.125$, flat land ($H_m^* = 0$ km), and no background wind ($U^* = 0\ \mathrm{m\,s}^{-1}$). These results are consistent with previous theoretical studies (e.g., Rotunno 1983; Qian et al. 2009; DR15), which refer to inertia–gravity waves excited by diurnal heating, which is the linear component of land–sea-breeze circulation within tropical regions. The waves are generated along the coastline, where the maximum thermal contrast occurs, and propagate as rays radiating upward into the atmosphere while simultaneously propagating both seaward and landward. Although the linear theory model developed in this study incorporates background wind effects, the current research focused solely on the impact of coastal terrain under zero background wind conditions, i.e., setting $U = 0$.

In the cases of mountain slope heating (Figs. 8b–d and 8f–h), coastal topography significantly alters the vertical wavelength of inertia–gravity waves compared to the flat coastal plain scenario. The dominant vertical wavelengths, indicated by the distance between purple solid and dashed lines, increase with larger $H_m^*$ (Fig. 8). The impact of topography is also evidenced by the amplitude of the gravity waves. In the flat coastal plain case, the maximum vertical motion peaks at approximately $0.03\ \mathrm{m\ s}^{-1}$. However, in the case with a 3-km mountain height, the maximum vertical motion exhibits a fourfold increase, exceeding $0.12\ \mathrm{m\ s}^{-1}$. These relationships align with our findings from the idealized experiments (Fig. 3), which demonstrated that mountain height has a positive linear correlation with both the vertical wavelength and amplitude of gravity waves.

Hovmöller diagrams of the vertical velocity averaged from 3 to 5 km AGL from the linear model are shown in Fig. 8. The propagation speed of the maximum vertical velocity is $10.0\ \mathrm{m\ s}^{-1}$ in the case of the flat coastal plain, increasing to approximately 11.0, 13.0, and $14.7\ \mathrm{m\ s}^{-1}$ with 1-km height and 2-km mountain and 3-km mountain slope heating, respectively. The phase speed of the inertia–gravity waves increases with mountain height, consistent with the findings from idealized simulations. The propagation speeds in the linear model cases closely match those of the idealized experiments shown

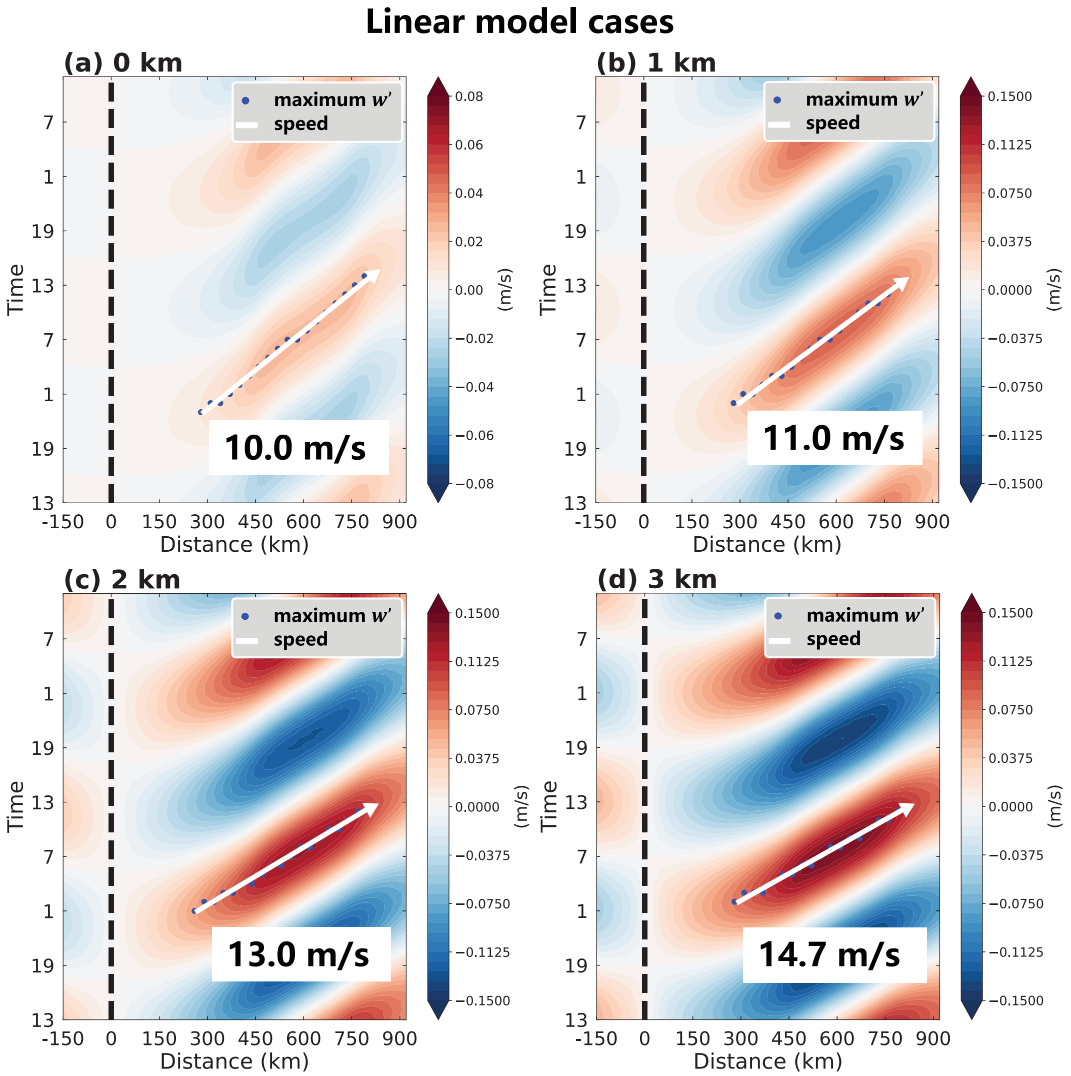

FIG. 9. As in Fig. 2, but for the linear model with (a) $H_m^* = 0$ km, (b) $H_m^* = 1$ km, (c) $H_m^* = 2$ km, and (d) $H_m^* = 3$ km.

in Fig. 2, with the largest differences within 0.5 m s$^{-1}$. These small discrepancies may result from minor ambiguities associated with our method of estimating phase speeds from Hovmöller diagrams. It is worth noting that the model estimates a propagation speed of approximately 13 m s$^{-1}$ for the case with 2-km mountain, which aligns well with the observed precipitation propagation speed from satellite data over the northern coast of New Guinea, where the average topographic height is about 2 km (not shown).

The horizontal phase speeds of the waves comprising the rays are governed by $c = \omega/k^* = \omega H/K = \omega H\sqrt{(N^2 - \sigma^2)\lambda_z^2/(f^2 - \sigma^2)}$, where $\lambda_z$ is the vertical wavelength of gravity wave [when $\lambda_z = 1/\gamma$ in (18)]. Consequently, the phase speed increases as the vertical scale becomes larger due to the thicker depth of the heating source near the coastline. As the heating depth increases, the vertical wavelength of the gravity waves also increases, echoing the earlier discussion. This result aligns with the findings from Li and Carbone (2015) in their linear model studies of elevated heating and land–sea-breeze cases. In addition to vertical wavelength, the horizontal phase speed of the wave also varies with $N$. According to the relation $c = \omega H\sqrt{(N^2 - \sigma^2)\lambda_z^2/(f^2 - \sigma^2)}$, the phase speed increases as $N$ increases. Moreover, the vertical variations in $N$ can significantly impact wave dynamics, leading to reflection and refraction of wave ray paths, particularly in layers where $N$ changes abruptly (Short et al. 2023; Du et al. 2024).

The maximum vertical motion of the wave in Fig. 9a is around 0.03 m s$^{-1}$, which is 0.07 m s$^{-1}$ smaller than that with 3-km mountain slope heating (Fig. 9d). It is intriguing to note that the vertical motion of the wave becomes stronger with a higher mountain slope, implying that the increased heating depth due to coastal mountains, with the same magnitude of forcing, plays a vital role in strengthening the wave perturbation. However, one evident difference in the phase of $w'$ here compared to the idealized cases (Fig. 2) is that the peak of $w'$ occurs at approximately 500–600 km from the coast (Fig. 9), which is about 150 km further than that in the idealized cases.

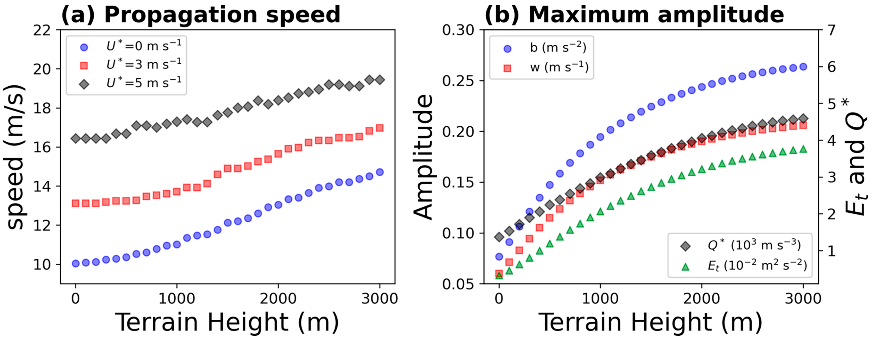

FIG. 10. Sensitivity of (a) the propagation speed and (b) maximum amplitude of gravity waves to coastal terrain height in the linear model. (a) Propagation speed of waves under three different background wind conditions (0, 3, and 5 m s$^{-1}$). (b) Maximum amplitude includes variations in vertical velocity $w$ (m s$^{-1}$), heating function $Q$ (m s$^{-3}$), buoyancy $b$ (m s$^{-2}$) variations, and total wave energy $E_t$ (m s$^{-2}$). The propagation speed is calculated from the vertical motion averaged from 3- to 5-km altitude range, as in Figs. 2 and 9.

This difference likely originates from two factors: 1) the vertical variation of the heating function in the linear model (cf. Figs. 7a,b), which is derived from the horizontally averaged vertical temperature profile of the nearshore land area in the idealized simulations, and 2) the absence of an actual mountain in the linear model. Additionally, the flow dynamics over the mountain in the idealized scenario may also contribute to this difference.

It is worth noting that the starting phase of the inertia–gravity waves in all the linear model cases has not changed significantly. This implies that the phase of waves is insensitive to the coastal topography in this linear model. This result contrasts with the findings of Li and Carbone (2015). In their study, which simulated the scenario of diurnal heating over mountains, they found that the starting phase of gravity waves occurs earlier with a larger heating depth in the elevated heating cases. This discrepancy may be due to the difference between the heating function in our linear model and the elevated heating cases in Li and Carbone (2015). In our coastal topography case, the heating function starts from the surface, while the elevated heating function in Li and Carbone (2015) starts from the top of mountain, with no heating source below the mountain top. Despite this, our results reveal the significant impact of coastal mountainous terrain on the vertical structure, phase speed, and intensity of inertia–gravity waves generated by diurnal heating.

### b. *Effects of coastal terrain*

We further quantitatively explore the influence of coastal mountainous terrain height on the propagation speed and maximum amplitude of inertia–gravity waves in the linear model (Fig. 10). The propagation speed increases slowly with terrain height up to 500 m and then exhibits a nearly linear rapid increase for heights between 500 and 3000 m. This suggests that the influence of low mountains (below 500 m) on the propagation speed of inertia–gravity waves is less pronounced than that of higher mountains (above 500 m). For flat or low coastal mountains, the land–sea thermal contrast likely dominates over the mountain–plain thermal contrast. Note that the increasing trend in speed shown in Fig. 10a is not entirely smooth, which may be attributed to variations in the objective method employed to calculate phase speed from the Hovmöller diagrams.

The influence of background wind on wave propagation is also shown in Fig. 10a. Through Doppler shifting, the propagation speed increases by approximately 3 and 5–6 m s$^{-1}$ when a background westerly winds of 3 and 5 m s$^{-1}$ are added, respectively, as discussed in Qian et al. (2009) and Du and Rotunno (2018). As topography height increases, the influence of background wind on wave speed still persists, which aligns with the Doppler shifting effect.

The maximum wave amplitude, which is represented by the magnitude of vertical velocity perturbations, also increases with terrain height (red dots in Fig. 10b) but at a gradually decreasing rate. The change is particularly small within the 2000–3000-m range. This can be attributed to the vertical variation of the heating function, which decreases with height as determined by the slope coefficient $a$ in (6). As shown in Fig. 7, Q is smaller at higher levels. Consequently, the vertical integration of $Q$ (black dots in Fig. 10b), which represents the total energy of the heating source, increases more slowly when $H_m^*$ exceeds 2000 m, resulting in a nonlinear increase of wave amplitude with terrain height. Noting that the total wave energy $E_t$ (green triangle markers in Fig. 10b), which includes kinetic and available potential energies, is proportional to the total heating energy $Q^*$. However, the heating function [(6)] is nonlinearly related to the topography height ($H_m^*$), and the total heating energy is not directly proportional to the terrain height. Therefore, the wave amplitude increases with terrain height in a manner that is not simply proportional to the terrain height. While the overall trends align with Li and Carbone (2015), the specific characteristics in our results exhibit notable differences from both their local elevated heating case and their land–sea-breeze case.

Both the propagation speed and amplitude increase with mountain height, consistent with the results discussed in idealized simulation. To gain deeper insight into these relationships through the linear analytical solution, the next section examines wave amplitudes at different horizontal wavenumbers.

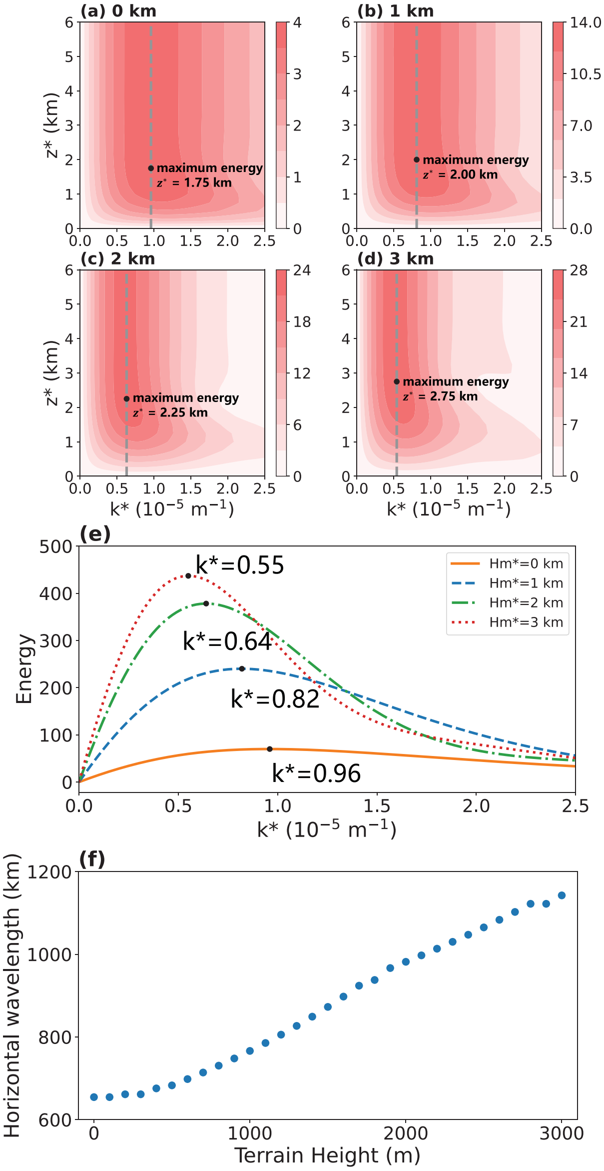

FIG. 11. Energy distribution as a function of height $z^*$ (m) and wavenumber $k^* = K/H$, calculated using the amplitude of the integrand $|-i\hat{\psi}K|$ from the linear model for (a) $H_m^* = 0\,\mathrm{km}$, (b) $H_m^* = 1\,\mathrm{km}$, (c) $H_m^* = 2\,\mathrm{km}$, and (d) $H_m^* = 3\,\mathrm{km}$. (e) Energy distribution in wavenumber $k^*$ after vertical integration from 3 to 5 km, computed using the amplitude of $\int_{3\mathrm{km}}^{5\mathrm{km}}|-i\hat{\psi}K|dz^*$ for different heights: $H_m^* = 0\,\mathrm{km}$ (orange line), $H_m^* = 1\,\mathrm{km}$ (blue line), $H_m^* = 2\,\mathrm{km}$ (green line), and $H_m^* = 3\,\mathrm{km}$ (red line). (f) Relationship between horizontal wavelength $\lambda_x$ and terrain height $H_m^*$, where $\lambda_x = 2\pi/k^*$ and $k^*$ is the wavenumber at the maximum amplitude of $\int_{3\mathrm{km}}^{5\mathrm{km}}|-i\hat{\psi}K|dz^*$. Gray dashed lines in (a)–(d) and black dots in (a)–(e) indicate the locations of maximum energy.

### c. *Characteristics of dominant waves*

Figures 11a–d illustrates the integrand $|-i\hat{\psi}K|$ as a function of $k^*$ and height $z^*$ from (34), representing wave amplitudes at different horizontal wavenumbers $k^*$ and heights $z^*$. The maximum wave amplitude, indicative of the dominant wave's energy, increases with mountain height, reaching a value of 28 for $H_m^* = 3\,\mathrm{km}$, compared to 4 for $H_m^* = 0\,\mathrm{km}$, consistent with the results shown in Fig. 10b. Moreover, in the flat plain case, the energy is spread across a wide range of $k^*$ values. In contrast, as the mountain height increases, the energy increasingly concentrates around the $k^*$ value of the dominant wave.

For $H_m^* = 0\,\mathrm{km}$, the maximum wave amplitude in the linear model occurs at $z^* = 1.75\,\mathrm{km}$ when $k^* = 9.6 \times 10^{-6}\,\mathrm{m}^{-1}$ (dominant horizontal wavenumber). As the mountain height $H_m^*$ increases, the height $z^*$ of maximum wave amplitude also increases. For instance, at the highest $H_m^* = 3\,\mathrm{km}$, the maximum amplitude occurs at $z^* = 2.75\,\mathrm{km}$, while the corresponding horizontal wavenumber $k^*$ decreases to $5.4 \times 10^{-6}\ \mathrm{m}^{-1}$. These results indicate that in cases with higher mountains, the dominant inertia–gravity waves are excited by higher altitude heating sources and exhibit larger horizontal wavelengths (smaller horizontal wavenumbers), even when the horizontal scale $x_0^*$ of the heating function remains constant. Moreover, the vertical wavelength also increases with mountain height, as depicted in Fig. 8. These findings demonstrate that thermal heating from coastal topography can significantly affect both the vertical and horizontal scales of inertia–gravity waves generated by diurnal heating.

As discussed in Du et al. (2024) and CD24, the horizontal phase speed of inertia–gravity waves $c = \omega/k^*$ is influenced by the horizontal wavenumber $k^*$. To examine the variation of $k^*$ for gravity waves in the 3–5-km layer, Fig. 11e depicts the vertical integral of the integrand $|-i\hat{\psi}K|$ from $z^* =$ 3-5 km, highlighting the horizontal wavenumber $k^*$ of the maximum energy wave (the dominant wave). In the flat coastal plain case, the $k^*$ value corresponding to the wave with the most energy is $9.6 \times 10^{-6}\ \mathrm{m}^{-1}$, while for the 1-km coastal mountain case, it decreases to $8.2 \times 10^{-6}\ \mathrm{m}^{-1}$ As the mountain height increases, $k^*$ of the dominant wave progressively decreases, reaching $5.5 \times 10^{-6}\ \mathrm{m}^{-1}$ for the 3-km mountain case.

Figure 11f presents results from a series of sensitivity tests examining the effects of terrain height and the dominant horizontal wavelength. Comparison of Figs. 10a and 11f reveals nearly identical trends: Both horizontal phase speed and the dominant horizontal wavelength increase with terrain height, confirming the direct relationship between these two factors. In other words, the height of coastal mountains influences wave energy distribution across different wavenumbers $k^*$. As the mountain height increases, energy tends to concentrate in waves with smaller $k^*$. When $k^* = HK$ and $\lambda_z = 2\pi/\gamma$ in (18), we obtain

$$\frac{2\pi}{\lambda_z} = H\sqrt{\frac{(N^2 - \sigma^2)k^{*2}}{f^2 - \sigma^2}}. \tag{35}$$

Thus, according to (35), the vertical wavenumbers $2\pi/\lambda_z$ are proportional to the horizontal wavenumbers $k^*$, suggesting that higher mountains, which generated the waves with larger vertical wavelength $\lambda_z$, correspond to dominant waves with smaller horizontal wavenumbers $k^*$. Consequently, this leads to faster horizontal phase speed ($c = \omega/k^*$) of inertia–gravity waves. The physical interpretation of these results is that the elevated heating effect of the terrain slope creates a deeper near-surface heating layer in the coastal area, which in turn generates gravity waves with a larger vertical scale. These findings are in alignment with both the idealized experiments in the present study and the more realistic simulations in CD24.

## 5. Summary and discussion

Coastal topography plays an important role in shaping the characteristics of diurnal rainfall propagation. CD24 suggests that the propagation speed of rainfall increases with faster phase speed of inertia–gravity waves due to greater heating depth from higher mountains near the coastline. This heating depth is closely related to the vertical scale of inertia–gravity waves, which in turn affects the phase speed of these waves and subsequently influences rainfall propagation. However, the mechanism by which coastal mountains alter the structure of inertia–gravity waves has not been well documented, partly due to challenges in isolating this effect in real scenarios, where numerous processes are involved. To address this, we employed an idealized numerical model and a linear analytical model to examine the influence of topography on inertia–gravity waves.

In this study, we compared a series of idealized WRF simulations with varying coastal terrain heights to isolate the impact of coastal mountains on inertia–gravity waves. By analyzing heating profiles near coastlines from these experiments, we developed a novel linear theory that combines the effects of land–sea and mountain–plain thermal contrasts. This theory incorporates averaged heating profiles from coastal mountain areas, elucidating the generation of gravity waves in mountainous coastal regions. The primary conclusions are as follows:

1) Compared to a flat coastal plain, the greater heating depth associated with higher coastal mountains affects both the vertical and horizontal wavelengths of inertia–gravity waves generated by diurnal heating. The increased vertical and horizontal scales of these waves result in higher phase speeds. In environments where offshore rainfall propagation is governed by gravity wave dynamics, greater heating depths consequently facilitate faster rainfall propagation. These processes are illustrated schematically in Fig. 12.
2) The greater heating depth from higher coastal mountains amplifies the amplitude of the inertia–gravity waves, causing stronger vertical motions and larger temperature anomalies along the wave ray paths.

From the analytical model, we obtained quantitative and detailed insights into the influence of coastal mountains on the characteristics of waves. Mountains lower than 500 m have a relatively minor effect on the propagation speed of inertia–gravity waves, while taller mountains produce more pronounced impacts. This is further evidenced by the trend in the horizontal wavelength of dominant waves as mountain height changes, reflecting the direct relationship between horizontal phase speed and horizontal wavelength. Due to the gravity wave dispersion relation, both parameters are influenced by variations in mountain height. As mountain height increases, the waves with dominant energy are excited at higher altitudes. Furthermore, with our choice of $Q$, the maximum amplitude of waves is evidently affected by coastal mountains up to 2 km in height but shows minimal change beyond this altitude.

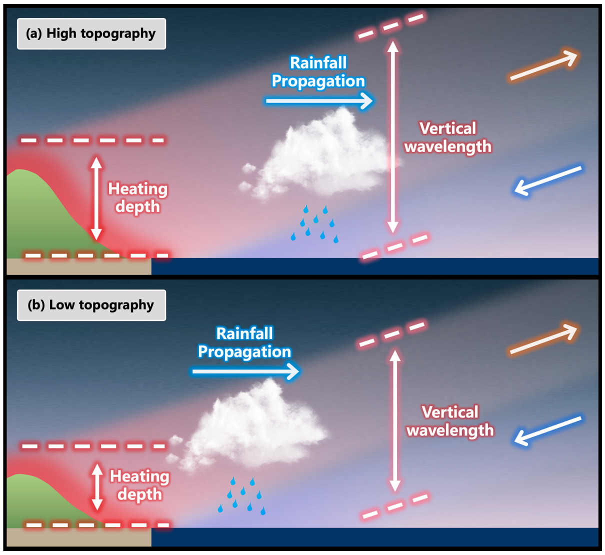

FIG. 12. Schematic illustration of the influence of coastal topography on gravity waves characteristics and offshore rainfall propagation. (a) High coastal topography results in a deeper heating layer, which generates gravity waves with longer vertical wavelengths. These waves propagate more quickly, leading to faster movement of rainfall. (b) Low coastal topography leads to a shallower heating layer, which generates gravity waves with shorter vertical wavelengths, leading to slower offshore propagation of both gravity waves and associated rainfall. The radial shading represents vertical motion.

Our linear theory successfully captures the changes in phase speed and structure of inertia–gravity waves observed in the idealized experiment. The heating effects of coastal mountains have been successfully incorporated into the linear theory of land–sea breezes (Rotunno 1983; Li and Carbone 2015; DR15; Du and Rotunno 2018), bringing the model closer to real-world scenarios where orographic effects of coastal mountain ranges are critical mechanisms in generating coastal precipitation (Aoki and Shige 2024). The analytical expressions derived from the linear model clearly demonstrate how wave characteristics change under the influence of coastal mountains.

Our study significantly advances the linear theory of coastal mountain–land–sea-breeze interactions, providing a more comprehensive understanding of these complex systems. While this study focuses on gravity wave dynamics, the findings of this study have important implications for understanding diurnal rainfall propagation. The wave characteristics identified in our linear model, particularly the propagation speed and its dependence on terrain height, provide physical mechanisms that help explain the observed rainfall propagation patterns in CD24.

Furthermore, the findings also have practical implications for both climate and meteorology. They can enhance the representation of tropical coastal rainfall in climate models, thereby enhancing the accuracy of rainfall projections for these regions. Additionally, this study provides valuable insights into interscale feedback mechanisms, contributing to a deeper understanding of how local topography influences large-scale atmospheric processes. Moreover, our results can refine models of phase-locked propagating systems (e.g., Ruppert and Zhang 2019; Ruppert et al. 2020) and aid in investigating cross-coastal impacts. Examples includes western Sumatra squall lines reaching Singapore, eastern Sumatra coast systems extending to eastern Borneo, and North Java coast systems propagating to southern Borneo (e.g., Short et al. 2019). These advancements have the potential to improve regional weather forecasting and climate modeling in complex coastal environments, ultimately enhancing our ability to understand and predict coastal weather phenomena.

In addition to topography, convective heating may also deepen the effective heating depth, thereby increasing phase speed in an analogous manner, as discussion by Hassim et al. (2016) and Vincent and Lane (2016). Other factors, such as latitude (Rotunno 1983), atmospheric stability (Jiang 2012a), and background winds (Qian et al. 2009; DR15), also influence propagation speeds by influencing $f$, $N$, and $U$ in the dispersion relationship. In contrast, deeper heating profiles affect wave rays and wave packets by altering the spectrum of excited waves.

However, our modeling experiments assumed a constant slope angle and a fixed distance of topography from the coastline. The linear theory applied in this study emulated the average heating associated with coastal mountains. We only examined scenarios where mountains are located near the coastline with the same slope angle as in CD24, without considering cases where mountains are situated at varying distances from the coast or have different slope angles. Both mountain location and slope angle can affect gravity wave generation and propagation. In addition, the effects of boundary layer processes and latent heat release from moist convection, which may influence wave behavior, are not included in the theoretical model. Boundary layer processes can modify the near-surface vertical temperature structure and the distribution of thermal contrast near slopes and coastlines, thereby affecting the generation and properties of gravity waves. Similarly, the latent heat release during convection may modify the heating depth of the source, which in turn changes the vertical scale and horizontal phase speed of the waves. These factors warrant further investigation in future studies.

It is important to note that the linear theory model developed in this study already incorporates background wind effects, although the current research focused on scenarios with zero and constant background wind. Future studies could extend this work to explore the influence of coastal mountains on gravity waves under various background wind shear conditions (e.g., Du et al. 2019) and distinct stability layers, such as the troposphere and stratosphere (e.g., Short et al. 2023; Du et al. 2024). Beyond coastal topography and background wind, other factors, such as boundary layer processes, diabatic heating from convective systems, other mesoscale processes such as cold pools or density currents, and complex coastline configurations in the real world, can affect the offshore propagation of precipitation (e.g., Love et al. 2011; Hassim et al. 2016; Vincent and Lane 2016; Peatman et al. 2023). Understanding the variability in propagation speeds remains a challenge and could be a focus for future research.

*Acknowledgments.* We are very grateful to three anonymous reviewers for their thoughtful suggestions and comments, which have greatly improved the quality of our manuscript. This study was supported by the National Key Research and Development Program of China (Grant 2024YFC3013003), the National Natural Science Foundation of China (42475002 and 42075006), the Guangdong Major Project of Basic and Applied Basic Research (2020B0301030004, 2024A1515510005, and 2025A1515011974), the Project supported by Southern Marine Science and Engineering Guangdong Laboratory (Zhuhai) (SML2024SP035, SML2024SP012, and 311024001), and the Key Innovation Team of the China Meteorological Administration (CMA2023ZD08). We also acknowledge the high-performance computing support from School of Atmospheric Sciences of Sun Yat-sen University.

*Data availability statement.* The model code and data in this study are available from the corresponding author upon request.

## REFERENCES

Aoki, S., and S. Shige, 2024: Control of low-level wind on the diurnal cycle of tropical coastal precipitation. *J. Climate*, **37**, 229–247, https://doi.org/10.1175/JCLI-D-23-0180.1.

Birch, C. E., S. Webster, S. C. Peatman, D. J. Parker, A. J. Matthews, Y. Li, and M. E. E. Hassim, 2016: Scale interactions between the MJO and the western Maritime Continent. *J. Climate*, **29**, 2471–2492, https://doi.org/10.1175/JCLI-D-15-0557.1.

Chen, Z., and Y. Du, 2024: The influence of topography on the diurnal rainfall propagation in the Bay of Bengal. *J. Atmos. Sci.*, **81**, 1019–1032, https://doi.org/10.1175/JAS-D-23-0225.1.

Du, Y., 2023: Offshore migration of summer monsoon low-level jet on a diurnal scale. *Geophys. Res. Lett.*, **50**, e2023GL103840, https://doi.org/10.1029/2023GL103840.

——, and R. Rotunno, 2015: Thermally driven diurnally periodic wind signals off the east coast of China. *J. Atmos. Sci.*, **72**, 2806–2821, https://doi.org/10.1175/JAS-D-14-0339.1.

——, and ——, 2018: Diurnal cycle of rainfall and winds near the south coast of China. *J. Atmos. Sci.*, **75**, 2065–2082, https://doi.org/10.1175/JAS-D-17-0397.1.

——, ——, and F. Zhang, 2019: Impact of vertical wind shear on gravity wave propagation in the land–sea-breeze circulation at the equator. *J. Atmos. Sci.*, **76**, 3247–3265, https://doi.org/10.1175/JAS-D-19-0069.1.

——, ——, Z. Chen, and H. Yang, 2024: A linear theory for periodic convectively forced gravity waves near a coastline. *J. Atmos. Sci.*, **81**, 1271–1288, https://doi.org/10.1175/JAS-D-23-0173.1.

Fang, J., and Y. Du, 2022: A global survey of diurnal offshore propagation of rainfall. *Nat. Commun.*, **13**, 7437, https://doi.org/10.1038/s41467-022-34842-0.

Halley, E., 1686: An historical account of the trade winds, and monsoons, observable in the seas between and near the Tropicks, with an attempt to assign the physical cause of the said winds. *Philos. Trans. Roy. Soc.*, **16**, 153–168, https://doi.org/10.1098/rstl.1686.0026.

Hassim, M. E. E., T. P. Lane, and W. W. Grabowski, 2016: The diurnal cycle of rainfall over New Guinea in convection-permitting WRF simulations. *Atmos. Chem. Phys.*, **16**, 161–175, https://doi.org/10.5194/acp-16-161-2016.

Houze, R. A., Jr., S. G. Geotis, F. D. Marks Jr., and A. K. West, 1981: Winter monsoon convection in the vicinity of North Borneo. Part I: Structure and time variation of the clouds and precipitation. *Mon. Wea. Rev.*, **109**, 1595–1614, https://doi.org/10.1175/1520-0493(1981)109<1595:WMCITV>2.0.CO;2.

Hu, X., J. Li, H. Chen, and R. Yu, 2024: Diurnal off-Mountain propagation of rainfall and low-level vertical velocity over the lee side of the Yungui Plateau. *J. Atmos. Sci.*, **81**, 1963–1976, https://doi.org/10.1175/JAS-D-23-0145.1.

Jiang, Q., 2012a: On offshore propagating diurnal waves. *J. Atmos. Sci.*, **69**, 1562–1581, https://doi.org/10.1175/JAS-D-11-0220.1.

——, 2012b: A linear theory of three-dimensional land–sea breezes. *J. Atmos. Sci.*, **69**, 1890–1909, https://doi.org/10.1175/JAS-D-11-0137.1.

Li, Y., and R. E. Carbone, 2015: Offshore propagation of coastal precipitation. *J. Atmos. Sci.*, **72**, 4553–4568, https://doi.org/10.1175/JAS-D-15-0104.1.

Love, B. S., A. J. Matthews, and G. M. S. Lister, 2011: The diurnal cycle of precipitation over the Maritime Continent in a high-resolution atmospheric model. *Quart. J. Roy. Meteoro. Soc.*, **137**, 934–947, https://doi.org/10.1002/qj.809.

Mapes, B. E., T. T. Warner, M. Xu, and A. J. Negri, 2003a: Diurnal patterns of rainfall in northwestern South America. Part I: Observations and context. *Mon. Wea. Rev.*, **131**, 799–812, https://doi.org/10.1175/1520-0493(2003)131<0799:DPORIN>2.0.CO;2.

——, ——, and ——, 2003b: Diurnal patterns of rainfall in northwestern South America. Part III: Diurnal gravity waves and nocturnal convection offshore. *Mon. Wea. Rev.*, **131**, 830–844, https://doi.org/10.1175/1520-0493(2003)131<0830:DPORIN>2.0.CO;2.

Mori, S., and Coauthors, 2004: Diurnal land–sea rainfall peak migration over Sumatera Island, Indonesian Maritime Continent, observed by TRMM satellite and intensive rawinsonde soundings. *Mon. Wea. Rev.*, **132**, 2021–2039, https://doi.org/10.1175/1520-0493(2004)132<2021:DLRPMO>2.0.CO;2.

Ogura, Y., and N. A. Phillips, 1962: Scale analysis of deep and shallow convection in the atmosphere. *J. Atmos. Sci.*, **19**, 173–179, https://doi.org/10.1175/1520-0469(1962)019<0173:SAODAS>2.0.CO;2.

Peatman, S. C., and Coauthors, 2023: The role of density currents and gravity waves in the offshore propagation of convection over Sumatra. *Mon. Wea. Rev.*, **151**, 1757–1777, https://doi.org/10.1175/MWR-D-22-0322.1.

Peng, C.-H., and X. Chen, 2023: Warm-season afternoon precipitation peak in the central Bay of Bengal: Process-oriented diagnostics. *J. Geophys. Res.*, **128**, e2022JD038398, https://doi.org/10.1029/2022JD038398.

——, and ——, 2024: Monsoonal MCS initiation, rainfall, and diurnal gravity waves over the Bay of Bengal: Observation and a linear model. *J. Atmos. Sci.*, **81**, 1401–1418, https://doi.org/10.1175/JAS-D-23-0230.1.

Qian, T., C. C. Epifanio, and F. Zhang, 2009: Linear theory calculations for the sea breeze in a background wind: The equatorial case. *J. Atmos. Sci.*, **66**, 1749–1763, https://doi.org/10.1175/2008JAS2851.1.

——, ——, and ——, 2012: Topographic effects on the tropical land and sea breeze. *J. Atmos. Sci.*, **69**, 130–149, https://doi.org/10.1175/JAS-D-11-011.1.

Rotunno, R., 1983: On the linear theory of the land and sea breeze. *J. Atmos. Sci.*, **40**, 1999–2009, https://doi.org/10.1175/1520-0469(1983)040<1999:OTLTOT>2.0.CO;2.

Ruppert, J. H., Jr., and F. Zhang, 2019: Diurnal forcing and phase locking of gravity waves in the Maritime Continent. *J. Atmos. Sci.*, **76**, 2815–2835, https://doi.org/10.1175/JAS-D-19-0061.1.

——, X. Chen, and F. Zhang, 2020: Convectively forced diurnal gravity waves in the Maritime Continent. *J. Atmos. Sci.*, **77**, 1119–1136, https://doi.org/10.1175/JAS-D-19-0236.1.

Sakaeda, N., and Coauthors, 2024: Synoptic influences on the diurnal cycle of rainfall over western Puerto Rico. *Mon. Wea. Rev.*, **152**, 2341–2359, https://doi.org/10.1175/MWR-D-24-0035.1.

Short, E., T. P. Lane, C. H. Bishop, and M. C. Wheeler, 2023: Diurnally forced tropical gravity waves under varying stability. *J. Atmos. Sci.*, **80**, 2557–2579, https://doi.org/10.1175/JAS-D-23-0074.1.

——, C. L. Vincent, and T. P. Lane, 2019: Diurnal cycle of surface winds in the Maritime Continent observed through satellite scatterometry. *Mon. Wea. Rev.*, **147**, 2023–2044, https://doi.org/10.1175/MWR-D-18-0433.1.

Skamarock, W. C., and Coauthors, 2008: A description of the Advanced Research WRF version 3. NCAR Tech. Note NCAR/TN-475+STR, 125 pp., https://doi.org/10.5065/D68S4MVH.

Sun, W.-Y., and I. Orlanski, 1981: Large mesoscale convection and sea breeze circulation. Part I: Linear stability analysis. *J. Atmos. Sci.*, **38**, 1675–1693, https://doi.org/10.1175/1520-0469(1981)038<1675:LMCASB>2.0.CO;2.

Vincent, C. L., and T. P. Lane, 2016: Evolution of the diurnal precipitation cycle with the passage of a Madden–Julian oscillation event through the Maritime Continent. *Mon. Wea. Rev.*, **144**, 1983–2005, https://doi.org/10.1175/MWR-D-15-0326.1.

Yang, G.-Y., and J. Slingo, 2001: The diurnal cycle in the tropics. *Mon. Wea. Rev.*, **129**, 784–801, https://doi.org/10.1175/1520-0493(2001)129<0784:TDCITT>2.0.CO;2.